

# Theoretical analysis of solar cell performance assisted by passive cooling



Cite as: Appl. Phys. Lett. 127, 103906 (2025); doi: 10.1063/5.0286585

Submitted: 20 June 2025 · Accepted: 12 August 2025 ·

Published Online: 11 September 2025



View Online



Export Citation



CrossMark

Qin Ye, Hongjie Yan, and Meijie Chen<sup>a)</sup>

## AFFILIATIONS

School of Energy Science and Engineering, Central South University, Changsha 430001, China

<sup>a)</sup>Author to whom correspondence should be addressed: [chenmeijie@csu.edu.cn](mailto:chenmeijie@csu.edu.cn)

## ABSTRACT

Passive cooling strategies, such as radiative cooling and evaporation cooling, have attracted lots of interest in the heat dissipation of solar cells. However, how to evaluate the effect of these passive cooling strategies on the solar cell performance was lacking, which is critical for the passive cooling design of solar cells. In this work, an electricity-thermal model was built to discuss the solar cell performance under different passive cooling conditions. Compared with the common solar cell with a glass cover, the sky radiative cooling by improving mid-infrared thermal emittance or above- $\lambda_g$  (effective cutoff wavelength) reflectance in the solar spectrum had a slight effect on the temperature drop or power improvement under natural convection. The core point was to ensure the near-perfect sub- $\lambda_g$  transmittance using anti-reflection coatings, which played the main role in the solar cell performance. A low cell temperature did not mean a high cell outpower under the selective spectral cover, and the sub- $\lambda_g$  transmittance could not be suppressed to improve heat dissipation performance. After introducing an evaporation cooling layer, the output power could be enhanced greatly, showing the wide adaptability to cool the solar cell with little effect on solar-to-electricity conversion efficiency in sub- $\lambda_g$  spectra. These results could guide subsequent cooling structure design by integrating different cooling strategies to achieve a near-perfect passive cooling system.

Published under an exclusive license by AIP Publishing. <https://doi.org/10.1063/5.0286585>

Solar cell cooling has attracted lots of attention recently, especially for passive cooling strategies,<sup>1,2</sup> such as thermal convection, radiative cooling, and evaporation cooling in Fig. S1. Sky radiative cooling could achieve zero energy cooling by reflecting solar radiation (0.3–2.5  $\mu\text{m}$ ) and emitting heat to the cold outer sky through the long-wave atmospheric transmittance window (LWIR in 8–13  $\mu\text{m}$ ),<sup>3–5</sup> which could be realized by dielectric and polymer scatters.<sup>6–8</sup> Radiative cooling attracts lots of interest in sub-ambient cooling,<sup>9,10</sup> water collection,<sup>11</sup> and outdoor heat dissipation.<sup>12,13</sup> For radiative cooling-assisted solar cell cooling, one structure was set as a common radiative cooling layer on the backside of the solar cell,<sup>14</sup> and a thermal reflector was placed below to reflect thermal radiation to the sky, which needed a complex optical system. The thermal reflector may also heat the radiative cooling layer. Another direct structure was designed as a selective spectral cover on the front side of the solar cell,<sup>15,16</sup> which should have high transmittance in sub- $\lambda_g$  (efficient cutoff wavelength), high reflectance in above- $\lambda_g$  of the solar spectrum, and high mid-infrared thermal emittance for radiative cooling.<sup>17</sup> This near-perfect metasurface cover was difficult to realize, which would inevitably reduce the sub- $\lambda_g$  transmittance.<sup>18</sup> How to balance the transmittance in sub- $\lambda_g$  and reflectance in above- $\lambda_g$  of the solar spectrum, and thermal emittance in the mid-infrared

region should be considered to maintain the perfect solar cell performance.<sup>19</sup>

In addition to the radiative cooling based on photonic design to cool the solar cell, evaporation cooling also provides a potential approach for solar cell heat dissipation,<sup>20,21</sup> which could release latent heat via evaporation to cool the cell in the daytime and capture water from the air in the nighttime.<sup>22</sup> The front side setup for evaporation cooling in the solar cell should maintain the high sub- $\lambda_g$  transmittance of the evaporation layer,<sup>23</sup> which could capture more water in the nighttime by radiation cooling-assisted adsorbent.<sup>24</sup> Usually, the evaporation layer can be set at the backside of the solar cell, which mainly captures water in the nighttime by adsorbent.<sup>25,26</sup> For example, a lightweight hydrogel was employed in silicon PV cell cooling, a temperature reduction of 23 °C was achieved (from 70 to 47 °C),<sup>27</sup> and an all-polymer polyethylene-hydrogel felt was also designed to reduce the temperature of solar cells by 28 °C under one sun.<sup>28</sup> Various passive cooling strategies have been designed for solar cells, such as radiative cooling, evaporation cooling, and so on. How to evaluate the effect of these strategies on the solar cell performance was lacking to guide structure design by integrating different cooling strategies in practical applications.

Hence, in this work, an electricity-thermal model was built to discuss the solar cell performance under different passive cooling strategies. For the solar cell in Fig. 1(a), the incoming energy flux comes from absorbed solar radiation ( $P_{\text{sun}}$ ) and atmospheric irradiation ( $P_{\text{atm}}$ ), and the outcome energy flux comes from heat dissipation by radiation ( $P_{\text{rad}}$ ), non-radiation ( $P_{\text{nonrad}}$ , i.e., thermal convection), and latent heat ( $P_{\text{latent}}$ , i.e., evaporation) to the environment. Here, the SunPower<sup>TM</sup> C60 solar cell [Fig. 1(b)] is used. Hence, the total energy balance equation can be described as follows:<sup>29</sup>

$$P_{\text{rad}} + P_{\text{nonrad}} + P_{\text{latent}} - P_{\text{sun}} - P_{\text{atm}} = 0, \quad (1)$$

where  $P_{\text{sun}}$  can be divided into two parts in terms of the effective cutoff wavelength  $\lambda_g = 1.2 \mu\text{m}$ . The above-bandgap photons can be converted into heat and electricity, while the sub-bandgap photons only produce redundant heat (i.e.,  $P_{\text{sun}} = P_{\text{heat}} + P_{\text{out}}$ ). Hence, in the solar spectrum, the ideal cover film in the solar cell system usually has high transmittance in the sub- $\lambda_g$  (0.3–1.2  $\mu\text{m}$ ), and high reflectance in the above- $\lambda_g$  (1.2–2.5  $\mu\text{m}$ ). In the mid-infrared spectra (>2.5  $\mu\text{m}$ ), it has a

high thermal emittance for heat dissipation in Fig. 1(c). Detailed power calculation can be found in [supplementary material S1](#).

The maximal electrical power of the solar cell  $P_{\text{out}}$  is attributed to short-circuit current density ( $J_{\text{sc}}$ ), open-circuit voltage ( $V_{\text{oc}}$ ), and fill factor (FF), which can be formulated as<sup>30</sup>

$$P_{\text{out}} = \text{FF} \cdot J_{\text{sc}} \cdot V_{\text{oc}}, \quad (2)$$

$$J_{\text{sc}} = \int_0^{\lambda_g} \frac{e\lambda}{hc} \cdot \text{EQE}(\lambda) \cdot \tau(\lambda) \cdot I_{\text{solar}}(\lambda) d\lambda, \quad (3)$$

$$V_{\text{oc}} = \frac{k_b T}{e} \cdot \ln \left( \frac{J_{\text{sc}}}{J_0} + 1 \right), \quad (4)$$

$$\text{FF} = n(1 - 1/y)(1 - \ln y/y), \quad (5)$$

where  $e$  is the electron charge.  $h$  is the Plank constant.  $c$  is the vacuum speed of light.  $k_b$  is the Boltzmann constant. Coefficient  $y = \ln(J_{\text{sc}}/J_0)$ .  $n$  is the correction factor. EQE is the external quantum efficiency [Fig. 1(d)], which can be calculated by  $\text{IQE}(\lambda) \cdot \alpha(\lambda)$ , where IQE is the inner quantum efficiency and  $\alpha$  is the absorptance of the solar cell

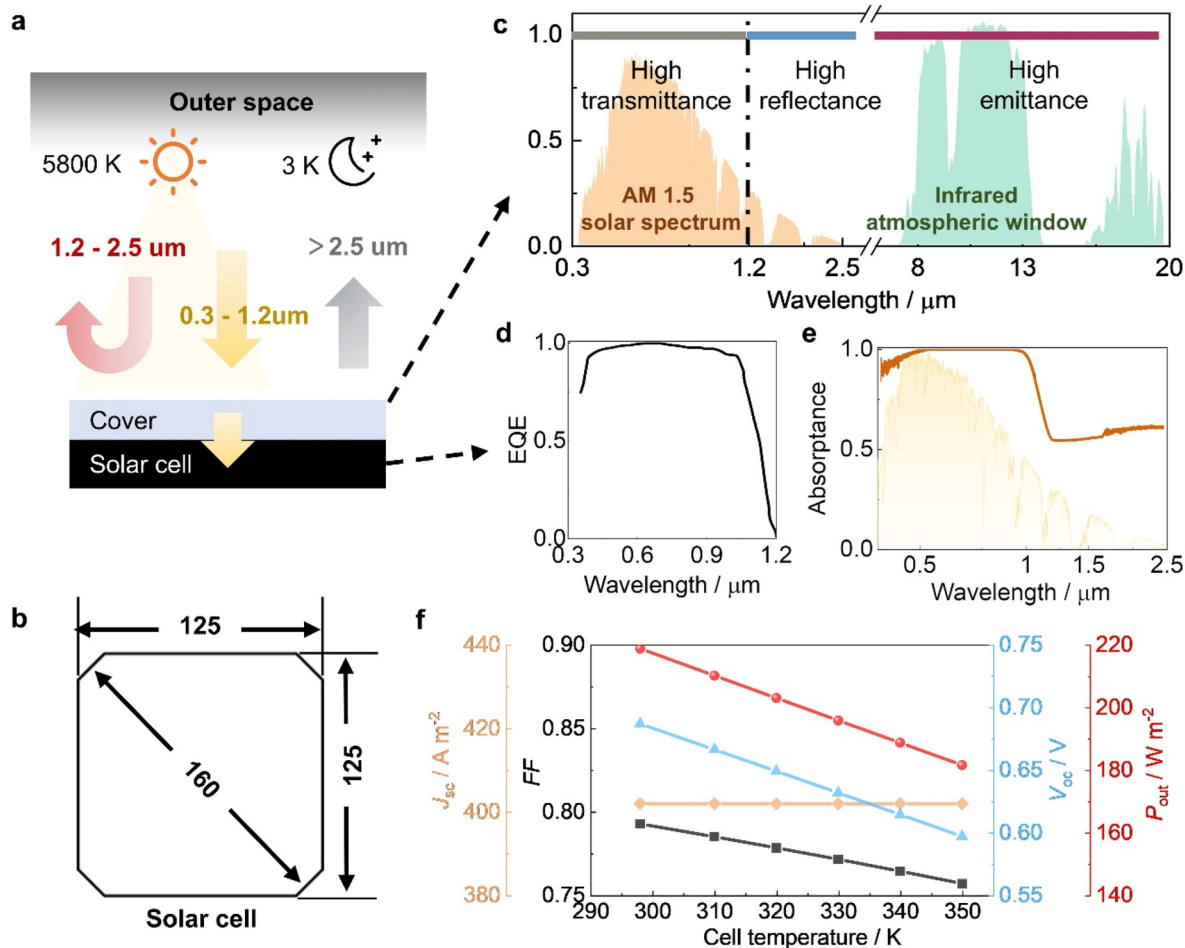


**FIG. 1.** Model description. (a) Schematic diagram of the solar cell with a selective spectral cover. (b) Geometry parameter of SunPower<sup>TM</sup> C60 solar cell (unit: mm). (c) Ideal spectra of cover. (d) External quantum efficiency and (e) measured spectral absorptance of the solar cell. (f) Calculated solar cell performance at different working temperatures.

**TABLE I** Comparison of testing data and calculated data for the SunPower<sup>TM</sup> C60 solar cell at standard test conditions: sunlight AM 1.5 and cell temperature 25 °C.

Verification	$P_{\text{out}}$ (W m <sup>-2</sup> )	Vol. drop (mV K <sup>-1</sup> )	Power drop (% K <sup>-1</sup> )
Testing data	219.9	-1.80	-0.32
Calculated data	218.9	-1.73	-0.33

[Fig. 1(e)].  $\tau$  is the transmittance of the cover on the front side of the solar cell. Detailed spectral measurement can be found in the supplementary material S2.  $J_0$  is the reverse saturation current for a PN junction (also known as the dark current of the solar cell), which can be calculated by

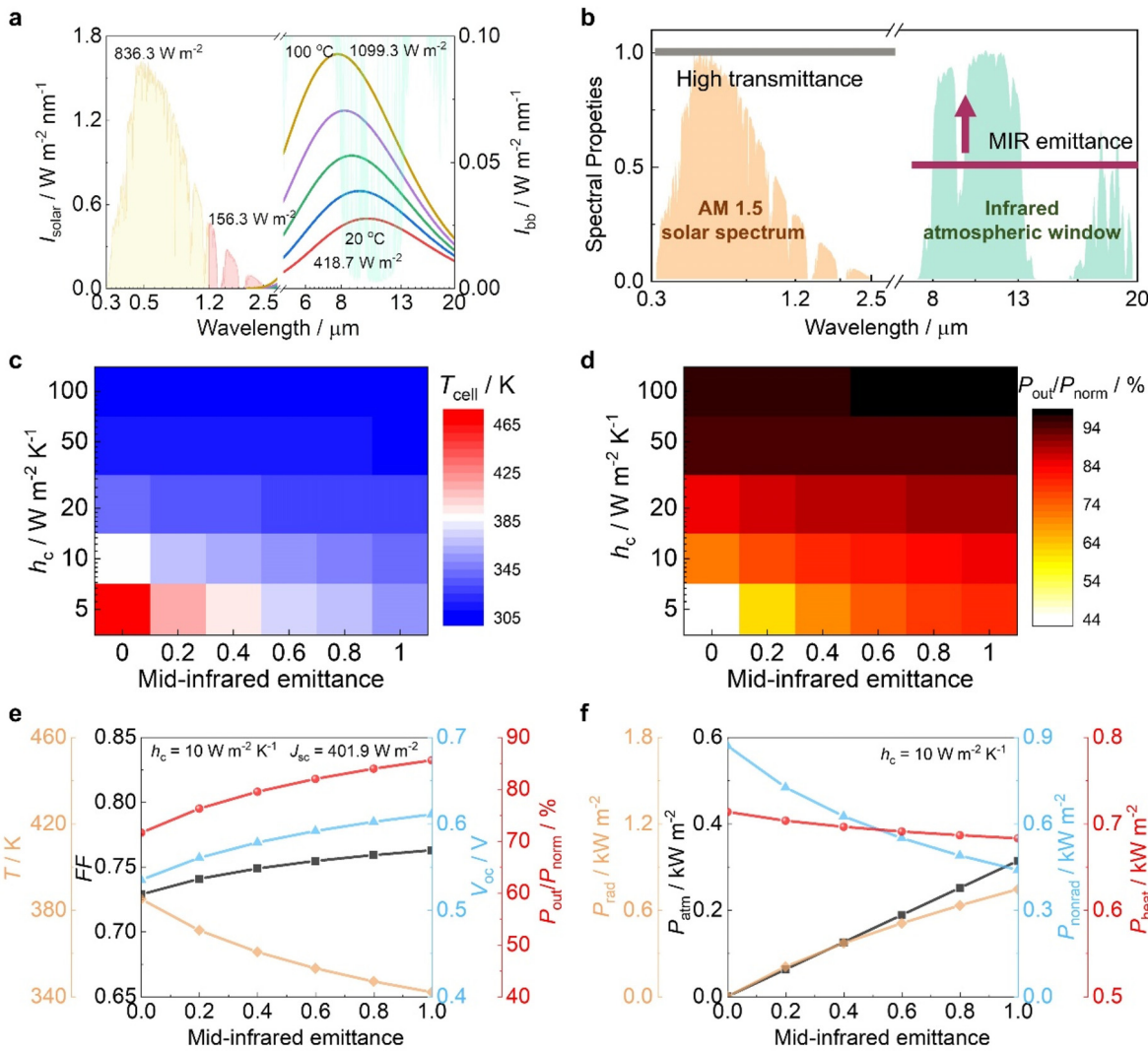


**FIG. 2.** Effect of mid-infrared (>2.5 μm) thermal emittance ( $\varepsilon_{\text{MIR}}$ ) on the solar cell performance. (a) Spectral solar intensity, atmospheric transmitted window, and blackbody spectral intensity. (b) Ideal spectra of the cover with different  $\varepsilon_{\text{MIR}}$ . (c) Cell temperature and (d) maximum output power ratio at different  $h_c$  and  $\varepsilon_{\text{MIR}}$ . (e) FF,  $V_{\text{oc}}$ ,  $J_{\text{sc}}$ , and  $T$ , and (f)  $P_{\text{rad}}$ ,  $P_{\text{nonrad}}$ ,  $P_{\text{atm}}$ , and  $P_{\text{heat}}$  at different  $t \varepsilon_{\text{MIR}}$  ( $h_c = 10 \text{ W m}^{-2} \text{ K}^{-1}$ ).

$$J_0 = e \left( \frac{D_n n_{p0}}{L_n} + \frac{D_p p_{n0}}{L_p} \right) = e n_i^2 \left( \frac{D_n}{L_n N_A} + \frac{D_p}{L_p N_D} \right), \quad (6)$$

where  $N_D/N_A$  is the donor/acceptor concentration.  $D_p/D_n$  is the hole/electron diffusion coefficient.  $L_h/L_e$  is the hole/electron diffusion length.  $n_{p0}/p_{n0}$  is the equilibrium minority carrier concentration in N/P region.  $n_i$  is the intrinsic carrier concentration of the solar cell. Assuming that  $D_p/D_n$  and  $L_h/L_e$  do not change with  $T$ ,  $J_0 \propto n_i^2 \propto T^3 \cdot \exp(-E_g/k_b T)$ , i.e.,  $J_0 = \gamma \cdot T^3 \cdot \exp(-E_g/k_b T)$ . Here,  $n$  and  $\gamma$  were estimated for the SunPower<sup>TM</sup> C60 solar cell. The ambient temperature is 298 K and solar intensity is 1 sun under AM 1.5.

Based on the built model, we calculated the solar cell performance under different working temperatures to verify its accuracy compared with the testing data for the SunPower<sup>TM</sup> C60 solar cell.<sup>31</sup> It can be

found that at the standard test conditions, the calculated power was similar to the product data (218.9 vs 219.9 W m<sup>-2</sup>) in Table I. In addition, the calculated outpower dropped with increasing cell temperature due to the weakened  $V_{oc}$  and FF in Fig. 1(f), and the calculated voltage drop and power drop were  $-1.73 \text{ mV K}^{-1}$  and  $-0.33\% \text{ K}^{-1}$ , which were similar to testing data ( $1.80 \text{ mV K}^{-1}$  and  $-0.32\% \text{ K}^{-1}$ ). These results indicate that the calculated model was valid to evaluate the solar cell performance under different heat dissipation conditions.

For the incident solar radiation, only photons smaller than  $1.2 \mu\text{m}$  can be transferred into electricity based on EQE, which accounts for  $836.3 \text{ W m}^{-2}$  in Fig. 2(a). Most of the absorbed solar radiation would generate heat to increase the cell temperature, and sky radiative cooling provides an approach to cool the solar cell via a high mid-infrared thermal emittance ( $\varepsilon_{\text{MIR}}$ ) in Fig. 2(b).

It can be found that the low thermal convection coefficient ( $h_c$ ) and  $\varepsilon_{\text{MIR}}$  would greatly increase the cell temperature, which was as high as  $472 \text{ K}$  at  $h_c = 5 \text{ W m}^{-2} \text{ K}^{-1}$  and  $\varepsilon_{\text{MIR}} = 0$  when the ambient

temperature ( $T_{\text{amb}}$ ) was  $298 \text{ K}$  in Fig. 2(c). Such a high-temperature increase ( $\Delta T = 174 \text{ K}$ ) led to a small output power of the solar cell ( $P_{\text{out}} = 96.7 \text{ W m}^{-2}$ ), which was only  $44.2\%$  of the output power at  $T_{\text{amb}} = 298 \text{ K}$  ( $P_{\text{norm}}$ ) in Fig. 2(d). In addition, at the low  $h_c$ ,  $\varepsilon_{\text{MIR}}$  played a critical role in improving the solar cell performance by sky radiative cooling. For example, at  $h_c = 5 \text{ W m}^{-2} \text{ K}^{-1}$ , the cell temperature could be dropped from  $472 \text{ K}$  at  $\varepsilon_{\text{MIR}} = 0$  to  $357 \text{ K}$  at  $\varepsilon_{\text{MIR}} = 1$ , improving the solar power from  $96.7$  to  $176.5 \text{ W m}^{-2}$ . While at the high  $h_c$ ,  $\varepsilon_{\text{MIR}}$  played a limited role due to the high heat dissipation performance via thermal convection. For example, at  $h_c = 100 \text{ W m}^{-2} \text{ K}^{-1}$ , the cell temperature only dropped from  $306.7 \text{ K}$  at  $\varepsilon_{\text{MIR}} = 0$  to  $305.2 \text{ K}$  at  $\varepsilon_{\text{MIR}} = 1$ , and the solar power changed little from  $212.6$  to  $213.7 \text{ W m}^{-2}$ .

At a typical  $h_c = 10 \text{ W m}^{-2} \text{ K}^{-1}$ , detailed solar cell parameters and energy fluxes at different  $\varepsilon_{\text{MIR}}$  can be found in Figs. 2(e) and 2(f), respectively. It can be found that  $J_{\text{sc}}$  was constant due to the constant incident solar radiation, while FF and  $V_{oc}$  increased with increasing

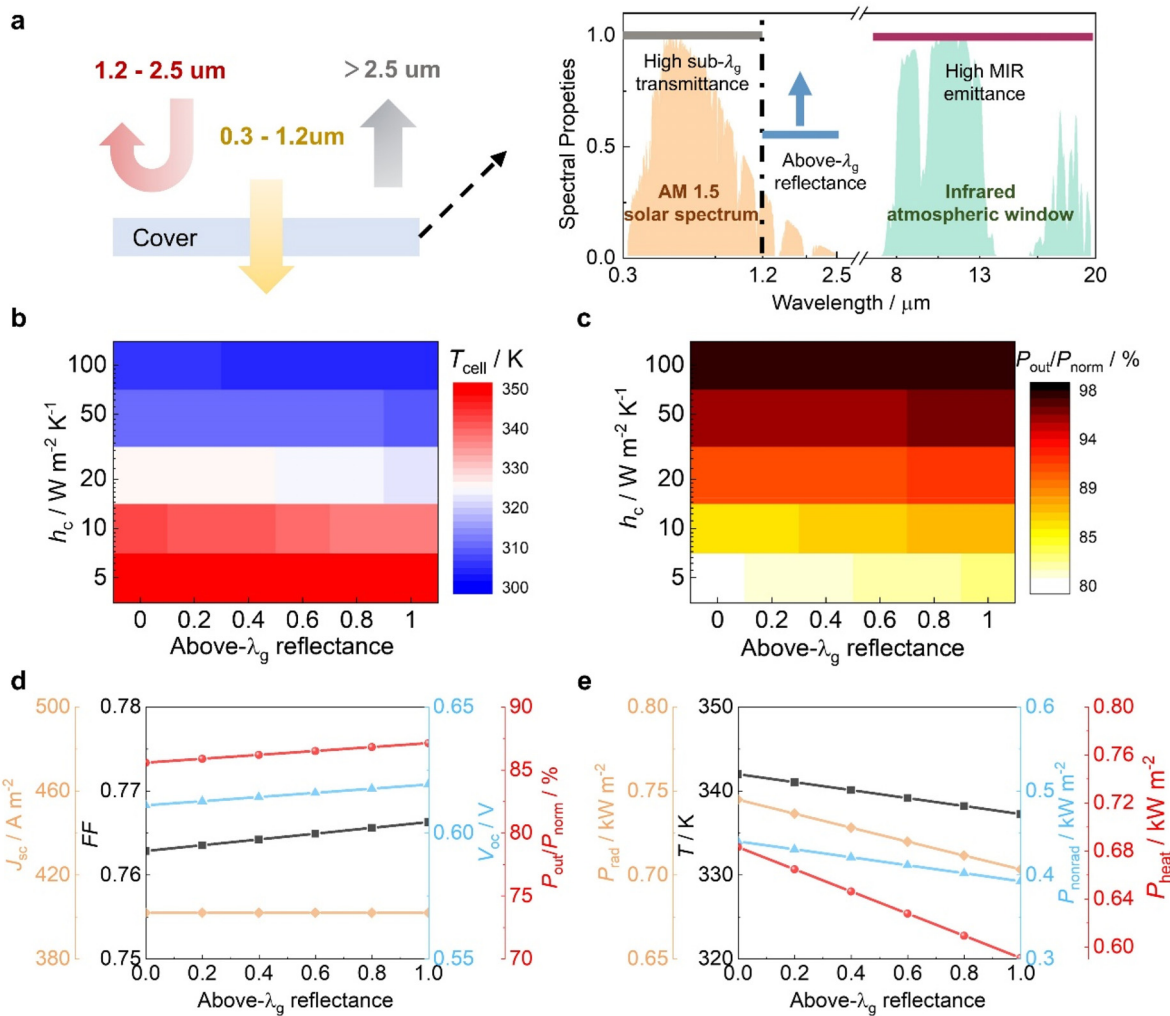


**FIG. 3.** Effect of above- $\lambda_g$  ( $1.2$ – $2.5 \mu\text{m}$ ) reflectance ( $\rho_{\text{above}}$ ) on the solar cell performance. (a) Ideal spectra of the cover on the solar cell with different  $\rho_{\text{above}}$ . (b) Cell temperature and (c) maximum output power ratio at different  $h_c$  and  $\rho_{\text{above}}$ . (d) FF,  $V_{oc}$ ,  $J_{\text{sc}}$ , and  $T$ , and (e)  $P_{\text{rad}}$ ,  $P_{\text{nonrad}}$ ,  $P_{\text{atm}}$ , and  $P_{\text{heat}}$  at different  $\rho_{\text{above}}$  ( $h_c = 10 \text{ W m}^{-2} \text{ K}^{-1}$ ).

$\varepsilon_{\text{MIR}}$  due to the decreased cell temperature, resulting in an increase in  $P_{\text{out}}$ . Both  $P_{\text{rad}}$  and  $P_{\text{atm}}$  increased with increasing  $\varepsilon_{\text{MIR}}$  although the cell temperature dropped.  $P_{\text{nonrad}}$  was weakened due to the decrease in the temperature difference ( $\Delta T$ ) while  $P_{\text{heat}}$  changed a little. Hence, increasing  $\varepsilon_{\text{MIR}}$  could improve the thermal radiation loss due to heat dissipation, resulting in a relatively low working temperature, especially at low  $h_c$ . However, the traditional common cover on the solar cell, such as glass, usually has a thermal emittance as high as  $>0.8$  in Fig. S2, which would only improve the solar cell power from  $183.8 \text{ W m}^{-2}$  at  $\varepsilon_{\text{MIR}} = 0.8$  to  $187.3 \text{ W m}^{-2}$  at  $\varepsilon_{\text{MIR}} = 1$  after a near-perfect photonic design.

In addition to sky radiative cooling, avoiding solar heating above- $\lambda_g$  spectra (i.e., high above- $\lambda_g$  reflectance in  $1.2\text{--}2.5 \mu\text{m}$ ,  $\rho_{\text{above}}$ ) also attracted lots of attention in solar cell cooling, which accounts for  $156.3 \text{ W m}^{-2}$  in Fig. 2(a). Hence, solar cell performance at different

$\rho_{\text{above}}$  was discussed in Fig. 3(a), where the near-perfect transmittance in sub- $\lambda_g$  and mid-infrared thermal emittance was used (i.e., equal to 1).

When  $\rho_{\text{above}}$  increased from 0 to 1, it had a slight effect on the temperature drop of the solar cell, which was only  $6.0 \text{ K}$  at  $h_c = 5 \text{ W m}^{-2} \text{ K}^{-1}$  and  $0.8 \text{ K}$  at  $h_c = 100 \text{ W m}^{-2} \text{ K}^{-1}$  in Fig. 3(b). Hence, a relatively larger power increase ( $4.2 \text{ W m}^{-2}$ ) could be achieved at  $h_c = 5 \text{ W m}^{-2} \text{ K}^{-1}$ , which was only  $0.6 \text{ W m}^{-2}$  at  $h_c = 100 \text{ W m}^{-2} \text{ K}^{-1}$  in Fig. 3(c). The high non-radiative heat dissipation would weaken the effect of radiative heat dissipation on the cell temperature. At a typical  $h_c = 10 \text{ W m}^{-2} \text{ K}^{-1}$ , detailed solar cell parameters and energy fluxes at different  $\rho_{\text{above}}$  can be found in Figs. 3(d) and 3(e), respectively. It can be found that  $J_{\text{sc}}$  was constant due to the constant incident solar radiation, while FF and  $V_{\text{oc}}$  increased with increasing  $\rho_{\text{above}}$  due to the decreased cell temperature, resulting in an increase in  $P_{\text{out}}$ .  $P_{\text{atm}}$

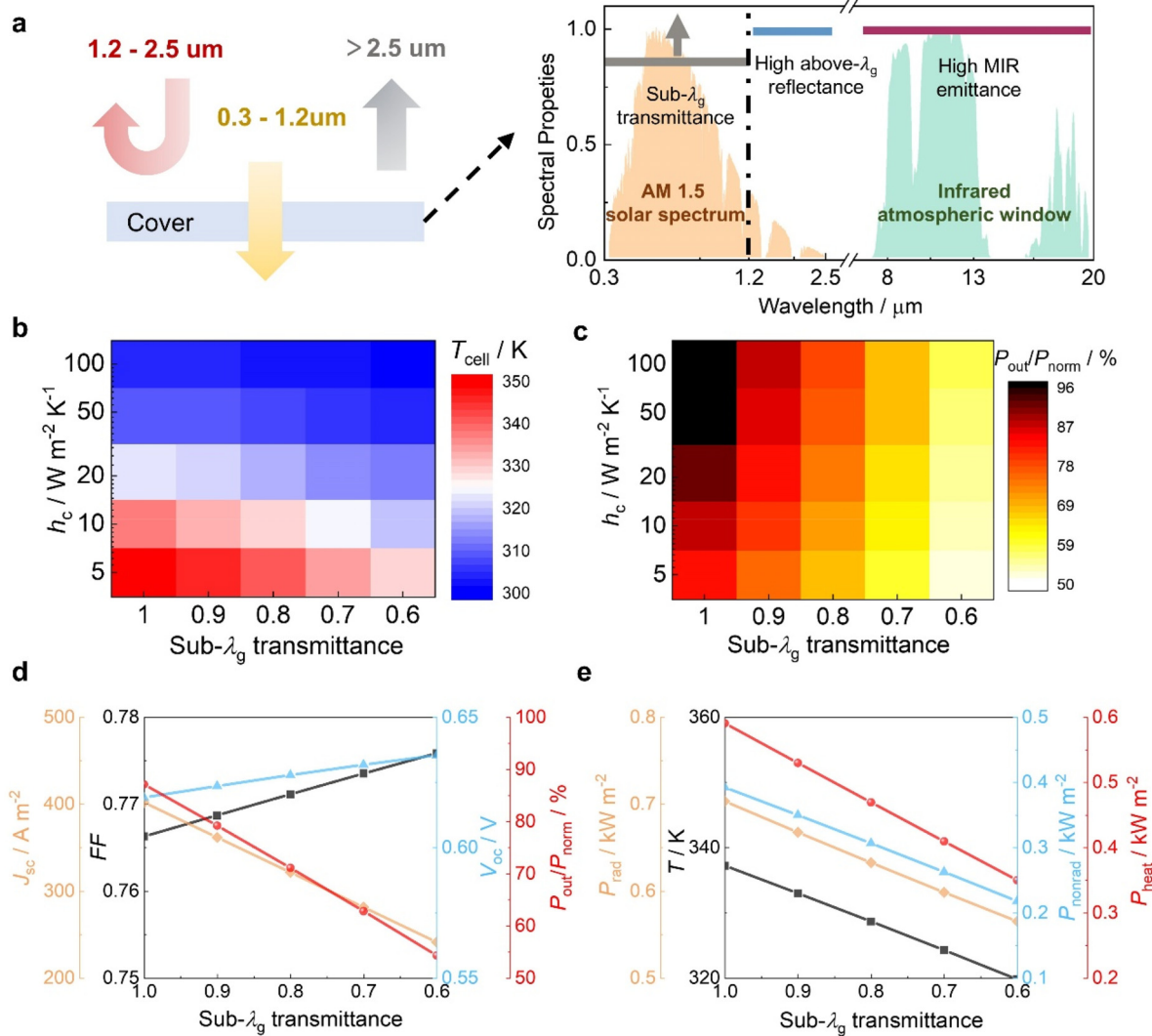


**FIG. 4.** Effect of sub- $\lambda_g$  ( $0.3\text{--}1.2 \mu\text{m}$ ) transmittance ( $\tau_{\text{sub}}$ ) on the solar cell performance. (a) Ideal spectra of the cover on the solar cell with different  $\tau_{\text{sub}}$ . (b) Cell temperature and (c) maximum output power ratio at different  $h_c$  and  $\tau_{\text{sub}}$ . (d) FF,  $V_{\text{oc}}$ ,  $J_{\text{sc}}$ , and  $T$ , and (e)  $P_{\text{rad}}$ ,  $P_{\text{nonrad}}$ ,  $P_{\text{atm}}$ , and  $P_{\text{heat}}$  at different  $\tau_{\text{sub}}$  ( $h_c = 10 \text{ W m}^{-2} \text{ K}^{-1}$ ).

was constant due to the constant meteorological parameters and mid-infrared thermal emittance. Both  $P_{\text{rad}}$  and  $P_{\text{nonrad}}$  decreased with the increased  $\rho_{\text{above}}$  due to the decreased cell temperature.  $P_{\text{heat}}$  also dropped due to the increased  $\rho_{\text{above}}$ . Hence, increasing  $\rho_{\text{above}}$  could drop  $P_{\text{rad}}$ ,  $P_{\text{nonrad}}$  and  $P_{\text{heat}}$ , resulting in an increase in  $P_{\text{out}}$  due to the decrease in cell temperature. However, at this typical  $h_c = 10 \text{ W m}^{-2} \text{ K}^{-1}$ , it only increased from  $187.3 \text{ W m}^{-2}$  at  $\rho_{\text{above}} = 0$  to  $190.7 \text{ W m}^{-2}$  at  $\rho_{\text{above}} = 1$ , and such perfectly selective spectra in solar spectra are also difficult to realize.

A high  $\rho_{\text{above}}$  in the above- $\lambda_g$  would inevitably weaken its sub- $\lambda_g$  transmittance in  $0.3\text{-}1.2 \mu\text{m}$  ( $\tau_{\text{sub}}$ ) in the practical design, which would suppress its solar cell performance. Hence, solar cell performance at different  $\tau_{\text{sub}}$  was discussed in Fig. 4(a), where the near-perfect reflectance in above- $\lambda_g$  ( $\rho_{\text{above}} = 1$ ) and mid-infrared thermal emittance ( $\varepsilon_{\text{MIR}} = 1$ ) were used. It can be found that the high  $\tau_{\text{sub}}$  would lead to a high working temperature and output power of the cell in Figs. 4(b) and 4(c). For

example, the maximum cell temperature ( $351.1 \text{ K}$ ) was achieved at  $\tau_{\text{sub}} = 1$  and  $h_c = 5 \text{ W m}^{-2} \text{ K}^{-1}$ , resulting in  $P_{\text{out}} = 180.8 \text{ W m}^{-2}$ . While the maximum output power of the cell was  $214.3 \text{ W m}^{-2}$  at  $\tau_{\text{sub}} = 1$  and  $h_c = 100 \text{ W m}^{-2} \text{ K}^{-1}$ , whose cell temperature was  $304.4 \text{ K}$ . For heat dissipation of the solar cell, just measuring the cell temperature drop was not enough to improve the cell performance.

At a typical  $h_c = 10 \text{ W m}^{-2} \text{ K}^{-1}$  in Figs. 4(d) and 4(e), with decreasing  $\tau_{\text{sub}}$ ,  $J_{\text{sc}}$  decreased due to the limited solar radiation on the cell surface, resulting in a decreased  $P_{\text{out}}$  although FF and  $V_{\text{oc}}$  increased due to the decreased cell temperature.  $P_{\text{atm}}$  was constant due to the constant meteorological parameters and mid-infrared thermal emittance. Both  $P_{\text{rad}}$  and  $P_{\text{nonrad}}$  were weakened due to the decrease in the temperature difference ( $\Delta T$ ), and  $P_{\text{heat}}$  also dropped due to the decrease in  $\tau_{\text{sub}}$ . Hence, decreasing  $\tau_{\text{sub}}$  could drop  $P_{\text{out}}$ ,  $P_{\text{rad}}$ ,  $P_{\text{nonrad}}$  and  $P_{\text{heat}}$ , resulting in a decrease in  $T$ ,  $J_{\text{sc}}$  and an increase in  $V_{\text{oc}}$ , FF. At this typical  $h_c = 10 \text{ W m}^{-2} \text{ K}^{-1}$ ,  $P_{\text{out}}$  would drop from  $190.7 \text{ W m}^{-2}$  at

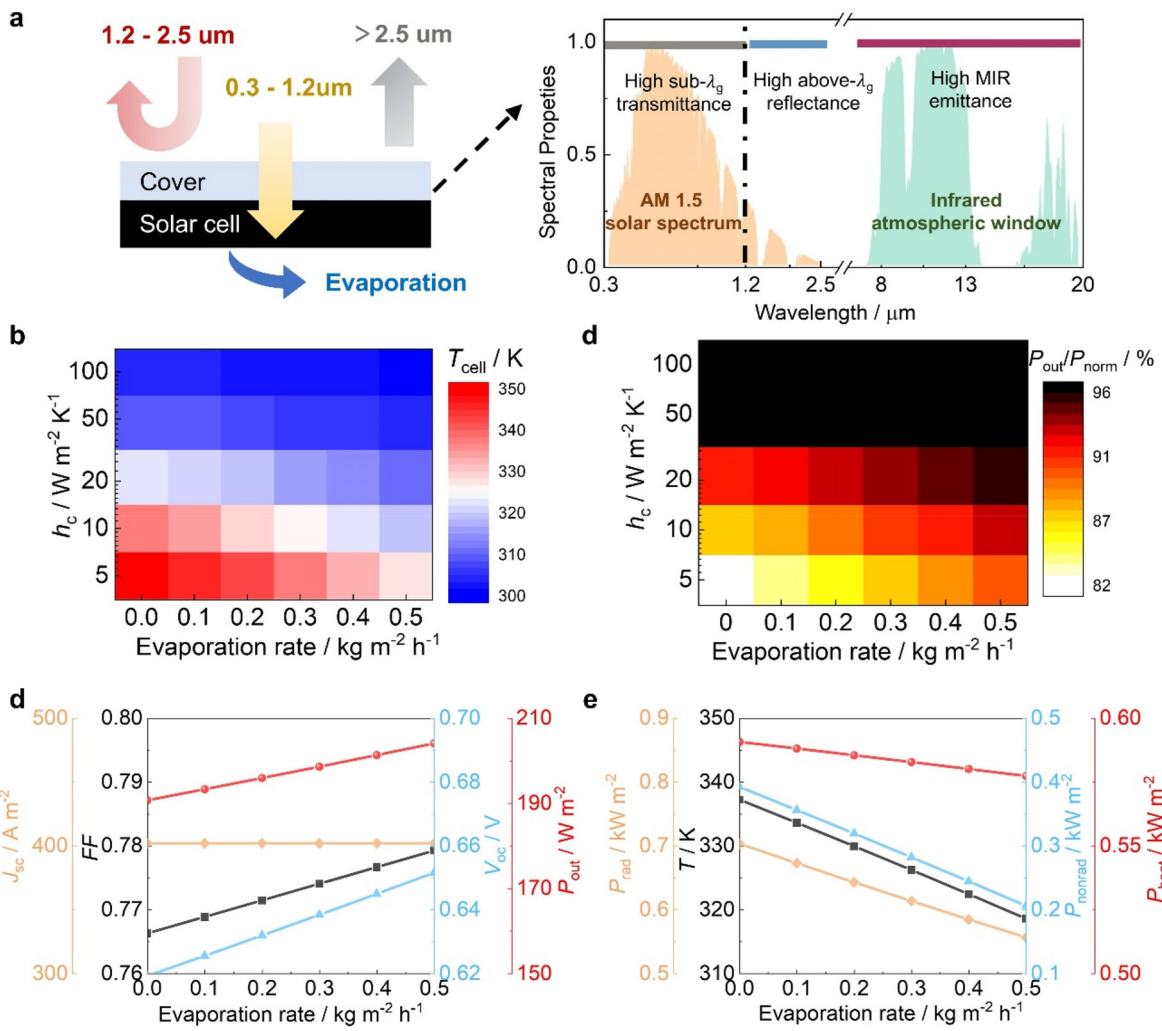


**FIG. 5.** Effect of evaporation cooling on the solar cell performance. (a) Ideal spectra of the cover on the solar cell with different evaporation rates. (b) Cell temperature and (c) maximum output power ratio at different  $h_c$  and evaporation rates. (d) FF,  $V_{\text{oc}}$ ,  $J_{\text{sc}}$ , and  $T$ , and (e)  $P_{\text{rad}}$ ,  $P_{\text{nonrad}}$ ,  $P_{\text{atm}}$ , and  $P_{\text{heat}}$  at different evaporation rates ( $h_c = 10 \text{ W m}^{-2} \text{ K}^{-1}$ ).

$\tau_{\text{sub}} = 1$  to  $155.7 \text{ W m}^{-2}$  at  $\tau_{\text{sub}} = 0.8$ . In the selective spectral design,  $\tau_{\text{sub}}$  should be enhanced by anti-reflecting coatings, which could not be suppressed to improve  $\rho_{\text{above}}$  in the solar spectrum.

In addition to the photonic design via sky radiative cooling, evaporation cooling provides another approach for passive cooling of the solar cell, which could improve the heat dissipation performance via evaporation in the daytime while capturing water from the air for water regeneration in the nighttime. Hence, solar cell performance at different evaporation cooling rates was discussed in Fig. 5(a), where the near-perfect transmittance in sub- $\lambda_g$  ( $\tau_{\text{sub}} = 1$ ), reflectance in the above- $\lambda_g$  ( $\rho_{\text{above}} = 1$ ), and mid-infrared thermal emittance ( $\varepsilon_{\text{MIR}} = 1$ ) were used. Evaporation cooling could greatly cool the solar cell. When the evaporation rate increased from 0 to  $0.5 \text{ kg m}^{-2} \text{ h}^{-1}$ , the cell temperature dropped  $24.3 \text{ K}$  from  $351.1 \text{ K}$  to  $326.8 \text{ K}$  at  $h_c = 5 \text{ W m}^{-2} \text{ K}^{-1}$ , which further weakened to  $3.2 \text{ K}$  from  $304.4 \text{ K}$  to  $301.2 \text{ K}$  at  $h_c = 100 \text{ W m}^{-2} \text{ K}^{-1}$  due to the enhanced radiative and convection losses in Fig. 5(b). Hence, a relatively large power increase ( $17.4 \text{ W m}^{-2}$ ) could be achieved at  $h_c = 5 \text{ W m}^{-2} \text{ K}^{-1}$ , which was only  $2.3 \text{ W m}^{-2}$  at  $h_c = 100 \text{ W m}^{-2} \text{ K}^{-1}$  in Fig. 5(c).

At a typical  $h_c = 10 \text{ W m}^{-2} \text{ K}^{-1}$ , detailed solar cell parameters and energy fluxes at different evaporation rates can be found in Figs. 5(d) and 5(e), respectively. It can be found that  $J_{\text{sc}}$  was constant due to the constant incident solar radiation, while FF and  $V_{\text{oc}}$  increased with increasing the evaporation rate due to the decreased cell temperature, resulting in an increase in  $P_{\text{out}}$ .  $P_{\text{atm}}$  was constant due to the constant meteorological parameters and mid-infrared thermal emittance. Increasing the evaporation rate could drop  $P_{\text{rad}}$ ,  $P_{\text{nonrad}}$ , and  $P_{\text{heat}}$ , resulting in an increase in  $P_{\text{out}}$  due to the decrease in cell temperature. At this typical  $h_c = 10 \text{ W m}^{-2} \text{ K}^{-1}$ ,  $P_{\text{out}}$  increased from  $190.7 \text{ W m}^{-2}$  to  $204.1 \text{ W m}^{-2}$  after introducing an evaporation cooling effect with a rate of  $0.5 \text{ kg m}^{-2} \text{ h}^{-1}$ . Usually, the evaporation cooling layer can be set on the backside of the solar cell without any effect on the photonic properties of the front side.

In conclusion, due to the high thermal emittance of the common cover used in the solar cell, such as glass, polymer, and so on, sky radiative cooling to improve the cell cooling performance was limited. Further photonic selective spectra design in the solar spectrum made it difficult to maintain the high transmittance in the sub- $\lambda_g$ , which would greatly drop the cell power by weakening its  $J_{\text{sc}}$ . On the front side of the cell, the core issue was to ensure the high transmittance in the sub- $\lambda_g$  by using the anti-reflection coating. Evaporation cooling on the backside of the cell provides an efficient passive cooling approach by the high latent heat of water, which could further regenerate water by atmospheric water harvesting (AWH) in the nighttime when the cell does not work. Detailed material and structure design are needed for this AWH medium to maintain its water capture and release in the all-day cycle, such as radiative cooling-assisted AWH. On the contrary, due to the interdependent heat and mass transfer processes in the passive cooling, developing multi-modes, such as radiative cooling, thermal convection, coupled evaporation cooling, could be a potential approach in the practical applications of solar cell cooling.

See the [supplementary material](#) for detailed calculation model, optical measurement, and supporting figures.

This work was financially supported by the Science and Technology Innovation Program of Hunan Province (No.

2024RC3003) and the Central South University Innovation-Driven Research Programme (No. 2023CXQD012).

## AUTHOR DECLARATIONS

### Conflict of Interest

The authors have no conflicts to disclose.

## Author Contributions

**Qin Ye:** Conceptualization (equal); Investigation (lead); Writing – original draft (lead). **Hongjie Yan:** Conceptualization (equal); Writing – review & editing (equal). **Meijie Chen:** Funding acquisition (lead); Supervision (lead); Writing – review & editing (equal).

## DATA AVAILABILITY

The data that support the findings of this study are available from the corresponding author upon reasonable request.

## REFERENCES

- <sup>1</sup>T. N. Sultan, M. S. Farhan, and H. T. H. Salim Alrikabi, "Using cooling system for increasing the efficiency of solar cell," *J. Phys.: Conf. Ser.* **1973**, 012129 (2021).
- <sup>2</sup>N. Guo, C. Shi, N. Warren, E. A. Sprague-Klein, B. W. Sheldon, H. Yan, and M. Chen, "Challenges and opportunities for passive thermoregulation," *Adv. Energy Mater.* **14**, 2401776 (2024).
- <sup>3</sup>M. Chen, D. Pang, J. Mandal, X. Chen, H. Yan, Y. He, N. Yu, and Y. Yang, "Designing mesoporous photonic structures for high-performance passive daytime radiative cooling," *Nano Lett.* **21**, 1412–1418 (2021).
- <sup>4</sup>X. Wang, X. Liu, Z. Li, H. Zhang, Z. Yang, H. Zhou, and T. Fan, "Scalable flexible hybrid membranes with photonic structures for daytime radiative cooling," *Adv. Funct. Mater.* **30**, 1907562 (2020).
- <sup>5</sup>C. Wang, H. Chen, and F. Wang, "Passive daytime radiative cooling materials toward real-world applications," *Prog. Mater. Sci.* **144**, 101276 (2024).
- <sup>6</sup>S. Liu, F. Zhang, X. Chen, H. Yan, W. Chen, and M. Chen, "Thin paints for durable and scalable radiative cooling," *J. Energy Chem.* **90**, 176–182 (2024).
- <sup>7</sup>M. Chen, D. Pang, X. Chen, H. Yan, and Y. Yang, "Passive daytime radiative cooling: Fundamentals, material designs, and applications," *EcoMat* **4**, e12153 (2022).
- <sup>8</sup>Z. Cheng, H. Han, F. Wang, Y. Yan, X. Shi, H. Liang, X. Zhang, and Y. Shuai, "Efficient radiative cooling coating with biomimetic human skin wrinkle structure," *Nano Energy* **89**, 106377 (2021).
- <sup>9</sup>W. Huang, Y. Chen, Y. Luo, J. Mandal, W. Li, M. Chen, C. C. Tsai, Z. Shan, N. Yu, and Y. Yang, "Scalable aqueous processing-based passive daytime radiative cooling coatings," *Adv. Funct. Mater.* **31**, 2010334 (2021).
- <sup>10</sup>Y. Liang, W. Zhang, H. Yang, J. Liu, Y. Zhou, H. Cui, and J. Yan, "Bridging the critical gaps of radiative sky cooling: From lab to applications," *Renewable Sustainable Energy Rev.* **222**, 115981 (2025).
- <sup>11</sup>M. Chen, J. Wang, S. Li, W. Chen, H. Yan, B. W. Sheldon, Q. Li, and C. Shi, "An all-passive and macro-patterned architecture design for water harvesting," *Nano Lett.* **24**, 16143–16150 (2024).
- <sup>12</sup>Q. Ye, X. Chen, H. Yan, and M. Chen, "Thermal conductive radiative cooling film for local heat dissipation," *Mater. Today Phys.* **50**, 101626 (2025).
- <sup>13</sup>Y. Liang, J. Liu, S. Zhang, Y. Du, H. Yang, H. Cui, and J. Yan, "Rethinking the role of thermal conductance in radiative sky cooling: Materials and applications," *Adv. Energy Mater.* **25**, 2500869 (2025).
- <sup>14</sup>Z. Wang, D. Kortge, J. Zhu, Z. Zhou, H. Torsina, C. Lee, and P. Bermel, "Lightweight, passive radiative cooling to enhance concentrating photovoltaics," *Joule* **4**, 2702–2717 (2020).
- <sup>15</sup>W. Li, Y. Shi, K. Chen, L. Zhu, and S. Fan, "A comprehensive photonic approach for solar cell cooling," *ACS Photonics* **4**, 774–782 (2017).

- <sup>16</sup>L. Zhu, A. Raman, K. X. Wang, M. A. Anoma, and S. Fan, "Radiative cooling of solar cells," *Optica* **1**, 32 (2014).
- <sup>17</sup>K. Wang, G. Luo, X. Guo, S. Li, Z. Liu, and C. Yang, "Radiative cooling of commercial silicon solar cells using a pyramid-textured PDMS film," *Sol. Energy* **225**, 245–251 (2021).
- <sup>18</sup>K. W. Lee, W. Lim, M. S. Jeon, H. Jang, J. Hwang, C. H. Lee, and D. R. Kim, "Visibly clear radiative cooling metamaterials for enhanced thermal management in solar cells and windows," *Adv. Funct. Mater.* **32**, 2105882 (2022).
- <sup>19</sup>B. Zhao, M. Hu, X. Ao, Q. Xuan, and G. Pei, "Spectrally selective approaches for passive cooling of solar cells: A review," *Appl. Energy* **262**, 114548 (2020).
- <sup>20</sup>L. Yu, Y. Huang, Y. Zhao, Z. Rao, W. Li, Z. Chen, and M. Chen, "Self-sustained and insulated radiative/evaporative cooler for daytime subambient passive cooling," *ACS Appl. Mater. Interfaces* **16**, 6513–6522 (2024).
- <sup>21</sup>L. Yu, Y. Huang, W. Li, C. Shi, B. W. Sheldon, Z. Chen, and M. Chen, "Radiative-coupled evaporative cooling: Fundamentals, development, and applications," *Nano Res. Energy* **3**, e9120107 (2024).
- <sup>22</sup>Q. Ye, D. Chen, Z. Zhao, H. Yan, and M. Chen, "Adhesive hydrogel paint for passive heat dissipation via radiative coupled evaporation cooling," *Small* **21**, 2412221 (2025).
- <sup>23</sup>S. Li, S. Wang, J. Zhao, Z. Wang, P. Murto, L. Yu, J. Chen, and X. Xu, "Spectrally-tailored hygroscopic hydrogels with Janus interfaces for hybrid passive cooling of solar cells," *Small* **25** 2505647 (2025).
- <sup>24</sup>Y. Huang, Q. Li, Z. Chen, and M. Chen, "Sorbent-coupled radiative cooling and solar heating to improve atmospheric water harvesting," *J. Colloid Interface Sci.* **655**, 527–534 (2024).
- <sup>25</sup>H. Li, J. Liu, J. Kang, C. Dong, X. Niu, L. Zhang, Y. Li, X. Meng, and W. Hong, "Encapsulated high-salt but corrosion-resistant hygroscopic medium for long-term passive solar cell cooling," *Small* **21**, 2408912 (2025).
- <sup>26</sup>Y. Liu, W. Xu, X. Zhou, A. Perwez, G. Qin, and X. Zheng, "Biomimetic thermo-responsive hydrogel coating for passive photovoltaic cooling via self-adaptive water management," *Small* **21**, 2502386 (2025).
- <sup>27</sup>T. Lapsirivatkul, S. Boon-in, D. Crespy, and P. Pattanasattayavong, "A light-weight hydrogel system for passive cooling of solar cells," *Adv. Mater. Technol.* **10**, 2401285 (2025).
- <sup>28</sup>K. Zheng, X. Fu, Y. Ren, Z. Yu, Z. Huang, J. Li, Y. Peng, C. Chen, and K. Liu, "All-polymer polyethylene-hydrogel felt for efficient evaporative cooling and ecological restoration in photovoltaic power plants," *Adv. Mater.* **25** 01698 (2025).
- <sup>29</sup>L. Yu, Z. Xi, S. Li, D. Pang, H. Yan, and M. Chen, "All-day continuous electrical power generator by solar heating and radiative cooling from the sky," *Appl. Energy* **322**, 119403 (2022).
- <sup>30</sup>K. Park, S. Basu, W. P. King, and Z. M. Zhang, "Performance analysis of near-field thermophotovoltaic devices considering absorption distribution," *J. Quant. Spectrosc. Radiat. Transfer* **109**, 305–316 (2008).
- <sup>31</sup>See [http://eshop.terms.eu/\\_data/s\\_3386/files/1379942540-sunpower\\_c60\\_bin\\_g-hi.pdf](http://eshop.terms.eu/_data/s_3386/files/1379942540-sunpower_c60_bin_g-hi.pdf) for solar cell parameters.